Temperature distribution during RF ablation on ex vivo liver tissue: IR measurements and simulations

Edoardo Gino Macchi · Mario Gallati · Giovanni Braschi · Alfredo Cigada · Lorenzo Comolli

Received: 30 April 2014 / Accepted: 22 September 2014 Published online: 30 September 2014

List of symbols

C_p	Specific heat at constant pressure (J/kg °C)
$\vec{n}$	Outward unit normal vector
$\dot{q}$	Joule heat per unit volume (J/m^3 s)
T	Time (s)
$t_{\max}$	Procedure duration (s)
V	Electric potential (V)
Z	Electrical impedance (Ω)

Greek symbols

α	Heat transfer coefficient (W/m^2 °C)
ε_r	Electrical resistivity (Ωm)
ε_r^{40}	Liver tissue electrical resistivity at 40 °C (Ωm)
θ	Temperature (°C)
θ_0	Initial temperature (°C)
θ^{amb}	Ambient temperature (air) (°C)
k_θ	Thermal conductivity (W/m °C)
ρ	Density (kg/m^3)

1 Introduction

Radiofrequency thermal ablation (RFTA) is a minimally invasive procedure widely adopted to treat liver cancer [1–3]. In addition, clinical applications of RFTA include treatment of kidney, lung, and prostate tumors, and painful soft tissue or bone masses that are unresponsive to conventional therapy [4–10]. Among the multiple techniques studied and used to kill tumor cells (laser, focused ultrasound, and microwave, cryotherapy, percutaneous ethanol injection), RFTA has emerged as safe, cheap, and quite predictable, and it is becoming the preferred treatment for small but inoperable liver tumors.

As well known, the procedure consists in necrotizing tumor cells in the liver tissue by means of the Joule heat

E. G. Macchi (✉) · M. Gallati · G. Braschi
Dipartimento di Ingegneria Civile e Architettura, Università degli Studi di Pavia, Via Ferrata 3, 27100 Pavia, Italy
e-mail: edoardogino.macchi01@ateneopv.it

A. Cigada · L. Comolli
Dipartimento di Meccanica, Politecnico di Milano, Via La Masa 1, 20156 Milan, Italy

developed by an electromagnetic field, applied by means of a RF generator between an active electrode, placed inside the volume to be treated, and an external passive electrode. Energy is thus deposed into the soft tissue: the heating rate is very high close to the active electrode and it rapidly decreases with distance. Above $\sim$60 °C proteins denaturation (and therefore cell death) takes place instantaneously [11, 12], when the boiling temperature is reached (depending upon the local pressure), the liquids start evaporating. The presence of vapor bubbles, close to the active electrode, breaks the electrical continuity and the procedure is automatically stopped.

The natural approach to assess the model performance consists in comparing results from numerical simulations with data obtained from experimental tests on ex vivo animal tissue [13–18]. The measurement of the temperature distribution is fundamental for the validation of any RFTA model since it is directly connected to the thermal lesion evolution, the main desired output of such model. Performing multiple temperature measurements during RFTA is not straightforward: most standard temperature measurement techniques are not well-suited, due to both electromagnetic interferences and the sensor heat sink effect. In most RFTA studies found in the literature tissue temperature has been measured only in 2-4 points (each at $\sim$5 mm distance) by using either thermistors or thermocouples [14, 18–20]. It is obvious that such measurements do not allow to accurately measure the temperature distribution, much less to estimate the temperature gradient. Theoretically the use of such sensors allows one to get the temperature time evolution at any specific point, however, from the practical point of view, it is nearly impossible to get a meaningful evaluation of the strong temperature gradients (up to 80 °C in 3 cm) with measurements in close points, due to sensor size and positioning. The miniature size of optical fibers allows monitoring along a single or multiple channels, ensuring a form factor that does not alter the sensing environment, however, in biomedical applications, the precise positioning of the sensors becomes quite difficult. Recent developments of draw-tower gratings (DTG) allow the realization of low-cost fiber Bragg grating (FBG) array on biocompatible, medical certified, ormoceramic fibers. An array with 5 FBG (0.5 cm active length, 1 cm between each FBG centre) has been recently tested for temperature monitoring during ex vivo RFTA [21]. While particularly promising, a further reduction of active length and an increase in sensing density are required for capturing the steep spatial temperature gradients induced by RFTA. The possibility of using a linearly chirped FBG for distributed temperature sensing during RFTA has also been recently investigated with tests on ex vivo liver tissue [22]; despite this approach seems promising, extensive validation of sensing system is necessary.

Infrared (IR) imaging is nowadays widely employed in medicine [23]: it has the advantage to provide field measurements without the "load" effects [24] due to the sensors presence affecting the system under measurement and it is insensitive to electromagnetic noise. However, the possibility of using a thermal camera for RFTA temperature monitoring is naturally limited to ex vivo analyses, where a direct line of sight is possible.

This paper describes some results from RF ablation tests, carried out on ex vivo porcine liver tissue, using a tip-like active electrode. The thermal field evolution, close to the active tip and inside the tissue were obtained by ther-mal imaging: the liver tissue temperature was measured with a spatial resolution $\leq$1 mm. Finally, the consistency of the measured data was checked through electro-thermal numerical simulations of the heating phase (up to 95 °C).

2 Experimental apparatus and procedure

2.1 Experimental strategy

The experiments must preserve the main features of the medical environment, such as space and time scales and the operational constraints: the RF generator, the power applied and the dimensions of the active electrode are similar to those employed in medical practice. Swine liver was employed, complying with EU ethic regulations. The liver specimens came from pigs slaughtered no more than 2 days earlier and were refrigerated until testing execution. Experiments were carried out at different power levels, kept constant through each test. The geometry of the "ideal" test setting is axisymmetric: the active electrode is placed at the center of a cylindrical tissue sample, with a volume large enough to ensure that the temperature increase near the lateral border (also acting as passive electrode) is negligible.

As mentioned above, performing temperature distribution measurements during RFTA is not straightforward: while IR imaging has the advantage to provide field measurements, the reference 3D cylindrical sample must be sectioned to get a clear line of sight to the emitting surface. Several different approaches can be adopted to choose the section plane and its interface with the surroundings. The 3D sample can be cut along the axial plane as well as along the equatorial plane while the sample surface can be left uncovered, to limit any energy filtering effect along the line of sight, or it can be protected with a thermally insulating lid (though as transparent as possible to the IR radiation). In case the free surface solution is adopted, significant thermal losses are introduced since heat and vapor can freely leave the sample. Moreover since water content dramatically changes during the procedure, the surface

emissivity might vary considerably. On the other hand, with the insulating lid, thermal losses are substantially reduced and the surface emissivity is unchanged.

A compromise solution was adopted: liver tissue temperature was measured only at some points, relying on an array of highly conductive thin nails piercing through the insulating lid. These nails produce a heat bypass from the tissue towards the outside only in a few points, therefore limiting energy losses and preserving the overall thermal balance. After a series of attempts with polycarbonate sheets (discarded because structurally anisotropic although semi-transparent), a balsa wood sheet equipped with small copper nails (diameter 0.6 mm) was adopted. The nails' temperature was measured by thermal imaging.

Concerning the section plane choice, two types of tests were carried out. The cylindrical sample was cut along the axial plane passing through the cylinder axis (AX setup) or along the equatorial plane (EQ setup). The AX setup, with free surface, allows one to display the thermal field evolution close to the active electrode during the procedure in both visual and IR fields. The EQ setup with the balsa wood lid, thanks to its minor energy losses and radial symmetry, is a better approximation of the reference 3D condition, as far as energy balance issues are concerned, so this solution is better suited for model calibration purposes.

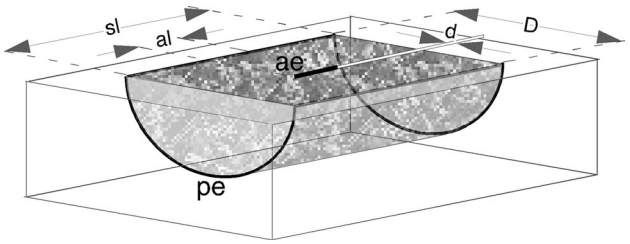

Fig. 1 Test box for AX setup; *ae* active electrode, *pe* passive electrode, $d = 4$ mm, $al = 20$ mm, $D = 80$ mm, $sl = \sim 100$ mm

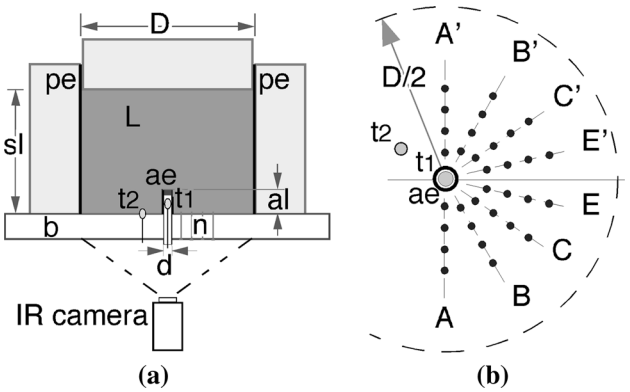

Fig. 2 Test box for EQ setup: **a** vertical cross section, **b** nails distribution (*upward zoomed view*). *ae* active electrode, *pe* passive electrode, *t*1–*t*2 thermistors, *L* liver, *b* balsa wood lid, *n* nails, $d = 4$ mm, $al = 10$ mm, $D = 80$ mm, $sl = \sim 50$ mm

2.2 Experimental setup

The test box for the AX setup is shown in Fig. 1. A hollow half cylinder having diameter *D* and length *sl*, was carved out of a single block of insulating material (extruded polystyrene, XPS). Porcine liver tissue (*L*) fills the box cavity. The active electrode (*ae*) is the tip of a thin brass tube (0.5 mm thick), having outer diameter *d* and length *al*, while the rest of the pipe is electrically insulated. It was placed along the cylinder axis, just below the tissue surface to ensure proper contact. A thermal sensor was placed inside the active electrode. The cavity wall was covered with a thin brass coating, acting as the passive electrode (*pe*). The liver tissue was arranged in the box with the liver capsule upside, to obtain a smooth free surface. With the above described test box laid down horizontally, videos were recorded from the top using an IR camera.

The test box for the EQ setup is shown in Fig. 2a; it is a hollow cylinder (diameter *D* and height *sl*) obtained from a block of XPS, with a removable top cover. The brass active electrode (*ae*) (diameter *d* and length *al*) is placed at the center of the balsa wood base (*b*) (10 mm thick) and it is equipped with a temperature sensor (*t*1). The box inner wall is coated with a thin metal sheet acting as the passive electrode (*pe*). A second temperature sensor (*t*2) is fixed to the base (*b*), also carrying the small copper nails (*n*), according to the mesh detailed in Fig. 2b. The figure also displays the position of active tip and temperature sensors and provides the nail numbering. The outer surface of the base (both nails and balsa wood) was painted black to get higher and more homogeneous surface emissivity. IR videos were recorded from the bottom. Special care was devoted to ensure the proper contact between liver tissue (previously heated at about 30 °C), active tip and nails. In order to ensure a better repeatability, tissue slices containing large blood vessels were not employed for the experiments.

Energy was supplied to the sample by means of a RF generator (TAG 100 W, Invatec, Roncadelle, Italy) that works within the impedance range 20–300 Ω: the power switch off is automatic, when the electrical load impedance exceeds 300 Ω. The frequency of the produced electromagnetic field is 480 kHz. Since the generator nominal power is usually different from the real power supplied to the sample, the latter was directly measured with the aid of an oscilloscope (DSO3062A Agilent, Santa Clara, CA, USA), a voltage probe (N2772A Agilent, Santa Clara, CA, USA) and a current probe (TCP305 Tektronix, Beaverton, OR, USA). Checks performed with saline, through calorimetric measurements, allowed to verify the reliability of the power values given by the oscilloscope: a systematic 5 % power reduction must be applied to obtain the real

power supplied to the sample. Since the sample impedance changes during both heating and vaporization, a manual feedback adjustment was needed to control the generator output to provide a constant power supply. At the end of the procedure the impedance undergoes a sudden and sharp increase, the automatic power off fixes the procedure duration ($t_{\max}$).

The main characteristics of the employed IR camera (Thermo Tracer TH7100 NEC, Tokyo, Japan) are: resolution 320 × 240 pixel, spectral band 7.5 to 13 μm, temperature range −20 to +120 ° C, uncertainty ±2 °C or ±2 % of reading, frame rate 10 Hz. The IR images were processed by means of custom developed Matlab® scripts. A temperature value was extracted from each pixel and, in EQ tests, the nail temperature was computed as the average of the pixels belonging to the area occupied by each nail.

The temperature measurements obtained using the IR camera may be subject to many uncertainty sources which are part of the measurement process and not just related to the IR camera uncertainty. Being conscious of the potentially large bias between the real temperatures and the measured values a proper uncertainty analysis was carried out [25]. The expanded uncertainty (k = 2) was 5.3 ° C providing a level of confidence of approximately 95 %. This depicts of course the worst scenario, but it provides at least a first uncertainty on the temperature estimation. Since the expanded uncertainty of the IR measurement system was quite high, a systematic check with NTC thermistors in spot points was carried out. NTC thermistors (B57861 Epcos, Munich, Germany) were chosen because they are less affected by electromagnetic noise than other traditional temperature sensors (e.g., RTDs, thermocou-ples) while offering high stability and a high degree of sensitivity. In addition to the sensor placed inside the active electrode, a second sensor was employed in EQ tests to check the IR measurements obtained from the nails. The NTC signals were acquired by National Instruments DAQ6008 board (National Instruments, Austin, USA) at a sampling rate of 100 Hz, high enough to capture the fastest transient.

2.3 Performed tests

The AX setup allow one to get the temperature field in all points of the exposed surface and to determine the temperature distribution along the tip and along lines normal to the stem axis; such information (although useless for the model calibration due to the significant thermal losses) help in specifying the evolution of the thermal field close to the active tip. The power supplied during test AX was 15 W. Tests EQ 15 and EQ 10 provide the radial temperature distributions that could be used for the calibration of a RFTA model. These tests too suffer from unavoidable minor heat losses (much lower than in the AX setup) thus the temperature distributions were slightly different along each radii. The real electric power (taking into account the 5 % power reduction) was about 14.2 and 9.5 W, respectively for tests EQ 15 and EQ 10. In order to check the replicability, the EQ tests were repeated seven times measuring only the active electrode temperature by means of the temperature sensor $t1$ (see Fig. 2). In addition two full 3D experiments (3D1–2) were carried out in a 3D box with the same diameter and double height (obviously at double power) with the purpose of checking the agreement between test EQ 15 and the reference 3D case. In 3D tests the required power was supplied by means of a stem electrode (same diameter and double active length).

3 Numerical model

3.1 Mathematical model

The mathematical model, briefly introduced here in after, is adequate for the simulation of the heating phase, while it requires some modifications to account for liquid–vapor phase change effects. The temperature θ is computed solving the heat equation:

$$\rho C_p \frac{\partial \theta}{\partial t} = \nabla \cdot (k_\theta \nabla \theta) + \dot{q} \tag{1}$$

where ρ, C_p and k_θ are respectively density, specific heat at constant pressure and thermal conductivity.

The source term (the heat produced by the Joule effect per unit volume) is computed as $\dot{q} = \frac{1}{\varepsilon_r} |\nabla V|^2$ where ε_r is the electrical resistivity and V is the electric potential.

Combining the continuity principle for the electric current and the local Ohm's law while adopting the "quasi-static" approximation for the electric field leads to the electric potential equation:

$$\nabla \cdot \left(\frac{1}{\varepsilon_r} \nabla V \right) = 0 \tag{2}$$

The electrical problem is solved at each time-step, to take into account the temperature dependence of liver tissue electrical resistivity. The solution allows one to compute the electrical impedance Z, which is the variable used to stop the power supply when its value exceeds the generator impedance upper limit (300 Ω) as it occurs in the experimental situation. According to our past experience the temperature dependence can be neglected for the thermal parameters, but it must be carefully considered for electrical resistivity, sensibly affecting the output results [14]. The liver tissue electrical resistivity temperature dependence was modeled using an experimental curve determined for ex vivo porcine liver tissue [14, 26].

3.2 Numerical method and boundary conditions

The equations of the mathematical model were discretized by means of the finite volume method using the C++library OpenFOAM® [27]. Equations (1) and (2) were solved with a fully implicit scheme to obtain the primary variables: θ and V. Second order accurate schemes were used for both time and space discretization.

The mathematical problem was solved with reference to an axisymmetric geometry. The unit 1 was discretized using about 18,000 hexahedral cells. The domain, bounded by the active and passive electrode and by the box walls, includes both active electrode and liver tissue. Appropriate electrical and thermal properties were assigned to the dif-ferent materials. The mesh was refined close to the active electrode where strong gradients of the primary variables are expected. After a sensitivity analysis on the mesh size and the time-step a cell scale ranging from 0.15 to 3.0 mm and a time-step of 0.5 s were selected.

The electric voltage equation was solved assigning, as boundary condition, a fixed voltage to both the active ($V = V^{ae}$) and the passive ($V = 0$) electrode, while a no-flux condition was imposed on the remaining boundaries. An iterative procedure is needed to compute the electric field with fixed power [14, 18] and to control that all the electrical power is supplied to the liver tissue, avoiding erroneous thermal sources due to discretization and interpolation schemes. Concerning the heat equation, no-flux boundary conditions were assigned to all boundaries except for the active electrode boundary, where following convective boundary condition (accounting for the heat losses) was imposed:

$$-k_\theta \nabla\theta \cdot \vec{n} = \alpha\left(\theta - \theta^{amb}\right) \tag{3}$$

where α is a heat transfer coefficient, θ^{amb} is the ambient temperature and $\vec{n}$ is the outward unit normal vector. A uniform initial temperature was set for the whole computational domain (30 °C for 15 W and 32 °C for 10 W).

3.3 Simulation parameters

The simulation employs physical parameters taken from literature [28–31] (see Table 1). The ambient temperature θ^{amb}, measured using a thermocouple, was 25 °C while the heat transfer coefficient α is set to 40 W/m °C.

All model parameters were kept constant through the simulation, as mentioned above, the liver resistivity was computed from the temperature using an experimental curve determined for ex vivo porcine liver tissue [14]. It prescribes a significant variation (about 55 % between 30 and 85 °C) following approximately a quadratic law [26]. The electrical resistivity of the brass active electrode is more than four orders of magnitude lower than the liver tissue resistivity; its exact value does not affect the simulation results and therefore is not reported.

Table 1 Physical parameters of liver tissue and brass active electrode: density ρ, specific heat at constant pressure C_p, thermal conductivity k_θ, liver tissue electrical resistivity at 40 °C ε_r^{40}

	ρ (kg/m^3)	C_p (J/kg °C)	k_θ (W/m °C)	ε_r^{40} (Ωm)
Liver tissue	1,050	3,400	0.6	3.0
Brass active tip	8,500	380	115	–

The physical variation of the liver tissue specific heat during heating was measured by several authors (e.g., [29, 30]) observing, in average, a 15 % increase at high temperatures. From the modeling point of view, such a variation is of minor importance, since its effects on the procedure outcome are quite limited.

The electro-thermal model previously described was used to simulate the EQ test experiments. Since the aim was to check the physical consistency of the experimental results obtained from the equatorial tests, the proposed mathematical model and therefore the simulation are limited to the heating phase (up to 95 ° C), the most deterministic part of the RF ablation procedure.

4 Results and discussion

4.1 Thermal field measurements: AX test

The IR measurements of the AX test allow one to qualitatively outline the thermal field development around the active tip. The temperatures were extracted along the active electrode (X direction) and along its symmetry axis (Y direction). Figure 3 displays the X and Y direction tissue temperature distributions during the heating phase, up to power switch off. For a better comprehension, the stem position is shown below the x-axis of each subplot. We remind that the stem was inserted into the tissue at a depth of about 2 mm and results were captured by thermal imaging, therefore, measurements are continuous through the tip region and the recorded temperatures are always lower than those recorded by the thermistor placed inside the active tip.

When the heating start (t = 10 s): two separate areas form (∼35 ° C), where the tip ends are positioned, these are not yet seen in the visible range. The temperature increase is slightly higher at the right-hand end, where the stem tip is located. This asymmetry is observed during the entire test. As heating continues, the temperature distribution gets more uniform along the active tip and the maxima at the two ends increase. (t = 42 s). In the visible range a

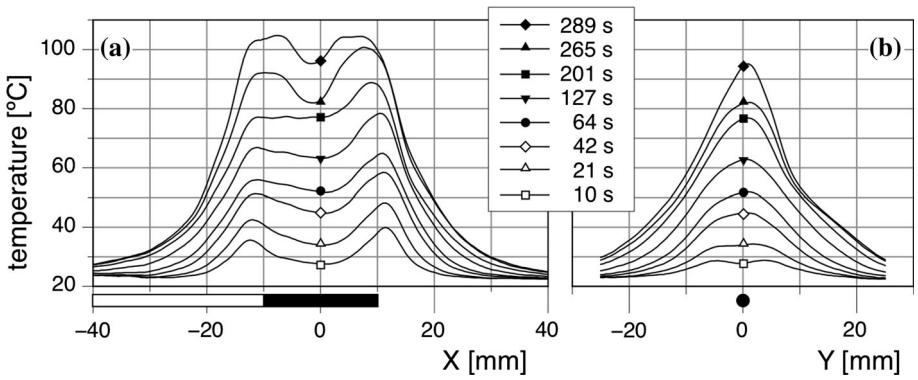

Fig. 3 Spatial distribution of temperature during heating (AX test, IR measurements): **a** *x direction*, along the active tip; **b** *y direction*, orthogonal to the active tip (and at X = 0 mm). The active electrode position is depicted below the x-axis

slight tissue color change due to tissue denaturation [12] starts being seen near the stem tip only when temperature reaches ~60 °C (t = 64 s). The heating continues regularly until liquid–vapor phase change begins. The electrical power is switched off when the active tip is surrounded by vapor (a good electrical insulator): two wider areas with temperature higher than 100 °C are detected. They are centered around the ends of the active tip, where the vapor inflates the tissue, as observed in the visible range.

The tissue temperatures measured in points along the tip help to understand the shape of the measured active tip temperature history. The active tip ends heat up at different rates: this behavior reflects the asymmetry of the thermal source spatial distributions and the stem heat sink effect. Despite the mean of the temperatures along the active electrode (from IR images) is lower than the NTC measurements inside the tip, a remarkable similarity in the trends of the two heating plots is noticed. This suggests that the active electrode temperature could be similar to the average temperature along the tip: use of thermal grease between sensor and active tip inner surface and the electrode material high thermal diffusivity support this hypothesis. The simulation results also confirm that the temperature inside the active tip is almost uniform due its high thermal diffusivity.

4.2 Temperature space–time evolution: EQ tests

The results of the equatorial experiments are summarized, in terms of duration and lesion diameter in the equatorial plane, in Table 2 together with the results of both AX and 3D tests. The lesion extension was identified by the change in color and consistence of the injured tissue, after the RF ablation procedure.

Figure 4 displays the active tip heating plots measured during the equatorial tests (EQ 15 and EQ 10): the measured data are represented with grey lines while their arithmetic mean is the thick black line (the bars represent the standard deviation). Concerning the mean curve, the continuous line part is computed as the average of the experiments, while the region close to the peak, represented by a dotted line, is computed normalizing the tests times (using the time of the temperature peak t_{max}) to keep the same plot shapes despite the different durations. In Fig. 4 the active tip temperatures from 3D tests (3D1-2) are also depicted for comparison.

Table 2 Equatorial, axial and 3D tests features and results: power, mean procedure duration (with standard deviation), mean lesion equatorial diameter (with standard deviation)

Test	Power (W)	Duration (s)	Lesion diameter (mm)
AX	15	289	21
EQ 15	15	114 ± 6	18 ± 1
3D	30	94 ± 8	18 ± 1
EQ 10	10	216 ± 28	20 ± 1

We observe that the procedure duration of EQ tests is longer than the full 3D tests; this can be explained by the absence of (small) thermal losses through the lid and by the thermal effects of the stem. Anyway the time scales of the procedure are comparable and the differences in duration are similar to those observed in repeated experiments. The active electrode temperature trends measured during EQ tests show that the results from different tests substantially agree up to 95 °C. The dispersion of results is lower for the 15 W tests (maximum standard deviation 2.8 °C) than for 10 W tests (maximum standard deviation 3.3 °C). Above 95 °C the plots change in shape, in a different way from test to test. From a physical point of view this behavior can be justified by the presence of vapor, quite sensitive to the tissue structural changes in the tip surroundings. The peak temperature exceeds 100 °C in all the performed tests, this leads to infer that the internal tissue pressure is higher than the atmospheric one, as expected during vaporization under almost isochoric conditions. In a first phase the tip temperature raises at a lower rate than during heating, then it increases with a steeper slope, presumably when the pressure starts raising, due to the increased energy density at

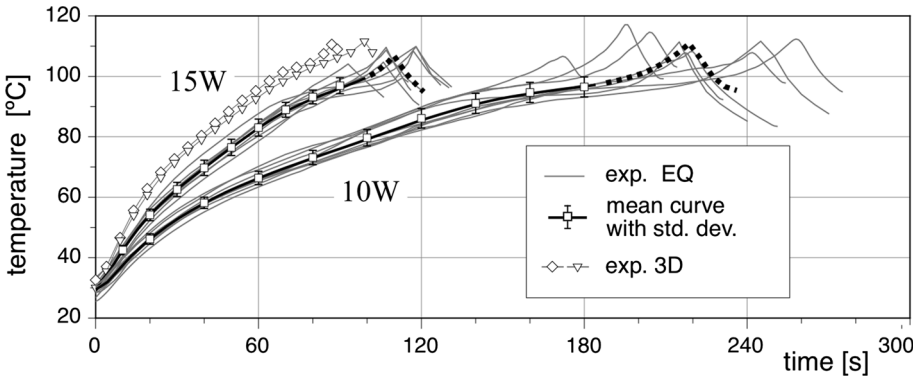

Fig. 4 Active tip temperature history: equatorial tests—15 W and 10 W (*grey lines*) and 3D tests (*lines with empty markers*). The mean active tip temperature histories of EQ 15 and EQ 10 experiments are also plotted (*thick black line*); the *error bars* represent the standard deviations

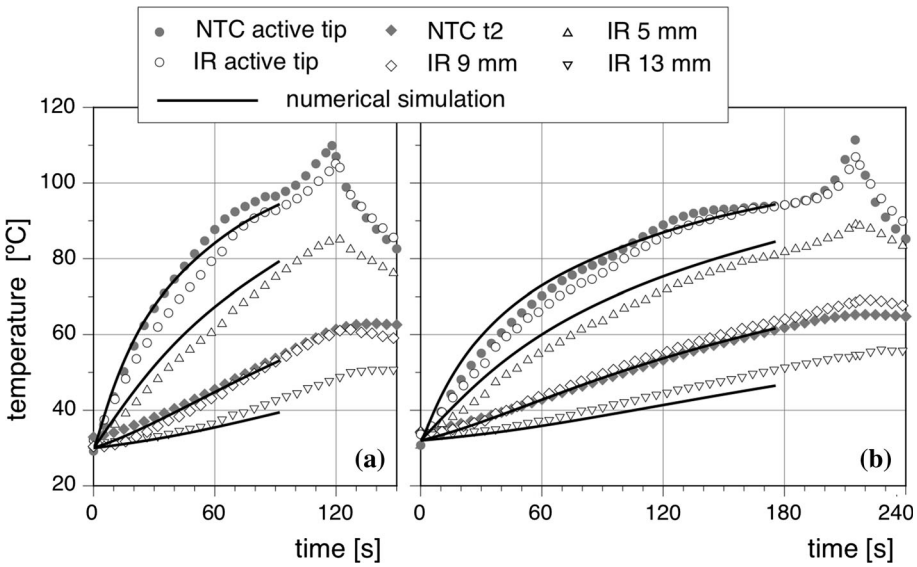

Fig. 5 Temperature histories at different radial positions: IR measurements (*empty markers*), NTC measurements (*filled markers*) and numerical simulations (*continuous line*): **a** EQ 15; **b** EQ 10. NTC and IR measurements are performed in similar positions

the center of the active tip, caused by the vapor presence at the ends.

Figure 5 shows the temperature histories measured from nails located at different radial positions from the tip (empty markers) together with the NTC measurements at position $t1$, inside the active tip, and at position $t2$ (filled markers). The simulation results are also plotted with continuous line.

NTC and IR temperature measurements performed at corresponding positions are in good agreement, nevertheless NTC measurements are always slightly higher. This is expected since NTC measurements are performed inside the active tip or inside the tissue while IR measurements are carried out on the surface of the nails. Anyway, the maximum difference is about 3 °C, which is lower than the expanded uncertainty of the IR measurement system, therefore we deduce that, despite the high uncertainty, the IR temperature measurements are reliable. The temperature peak observed at the end of the procedure near the active electrode is not perceived at distances greater than 5 mm from the tip. We argue that probably these regions are scarcely affected by the phase change effects. In EQ 10 tests the heating rate sensibly decreases over 95 ° C and vaporization lasts longer, this suggests that the hypothesis of isothermal/isobaric vaporization is more suited to model the phase change when RFTA is performed at low power. Regarding the radial temperature distribution, for every EQ test, eight radial distributions can be obtained at homologous radii with respect to the symmetry axis of the nail mesh (see Fig. 2). The measured temperature trends are sensibly smooth along each radius and define a com-mon average radial gradient. The radial temperature distributions measured in tests EQ 15, at four characteristic times ($1/6t_{max}$, $1/4t_{max}$, $1/2t_{max}$ and t_{max}), are depicted in Fig. 6, where values from homologous radii, considering symmetry with respect to the nail distribution axis (A–A′, B–B′, etc.), have been averaged. The simulation results corresponding to the first three times (those belonging to the heating phase) are also plotted for comparison. The temperature distributions recorded during tests EQ 15 and

EQ 10, at the same fractional time (t/t_{max}), are quite similar: the differences are highlighted in Fig. 7, where the simulations results are also reported.

4.3 Simulation results and discussion

In this work numerical simulations are used to check the consistency of the performed temperature measurements. The simple mathematical model previously described is suitable for modeling the heating phase of the procedure, before the vaporization begins.

The results of the numerical simulations are reported in Figs. 5, 6 and 7 together with the experimental measurements. The numerical simulation suitably reproduces the temperature history trend at different distances from the tip (Fig. 5); the simulated temperature at 5 mm and 13 mm is respectively slightly higher and lower. The model radial temperature distributions are in good agreement with the IR measurements (Figs. 6, 7): the average coefficient of determination (R^2) is about 0.93 for 15 W test and 0.90 for 10 W test.

The general acceptable agreement obtained with literature physical parameters and neglecting the lid thermal losses proves the overall consistency of the measured data. While the electrical resistivity variation with temperature is essential to correctly model the RFTA procedure, it appears that a constant thermal conductivity model can satisfactorily reproduce the temperature gradients.

In conclusion both experimental evidences and modeling suggest that the measured radial temperature distributions are a meaningful approximation of the reference 3D situation and thus can be employed for the calibration of a more complex RFTA model. Such model must take into account both thermal and electrical effects of liquid–vapor phase change to correctly reproduce the entire RF ablation procedure.

RF ablation is usually performed under ultrasound guidance which only enables to approximately identify the ablated region: the physician adjusts the power output, frequently based on his previous experience, in order to treat the tumor (plus, whenever possible, a 5–10 mm safety margin) while preserving healthy tissue. In the last years the increase in computational power allowed to perform patient specific RFTA treatment planning using numerical simulations. However RFTA treatment planning is not yet widespread because of its complexity and because patient specific tissue properties should be determined to optimize its accuracy [32, 33]. Nevertheless numerical simulations can be used to assess the treatment strategy (e.g., choice of type of elec-trode, optimal power regulation, saline injection) and to study ways to further improve the RFTA procedure.

While the calibration of RFTA models is usually based on ex vivo experiments, this situation omits blood perfusion, one of the most important factors affecting the in vivo procedure outcome. Modeling blood perfusion entails some serious difficulties: the commonly used Pennes model [34–38] simply adds a fictitious volumetric heat sink to the heat equation however the blood flow directionality and the related convective heat transport are

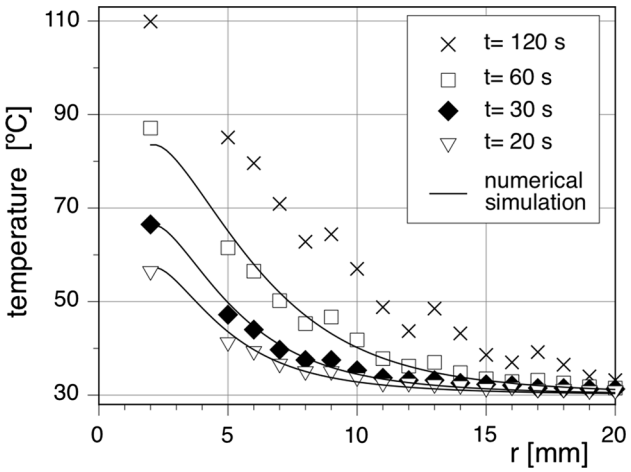

Fig. 6 Radial temperature distributions from tests EQ 15 at four characteristic times: nails IR measurements (*markers*) and numerical simulation (*continuous line*). Since numerical modeling is limited to the heating phase, the simulated temperature distribution during liquid–vapor phase change, just before the end of the procedure (t = 120 s), is not represented

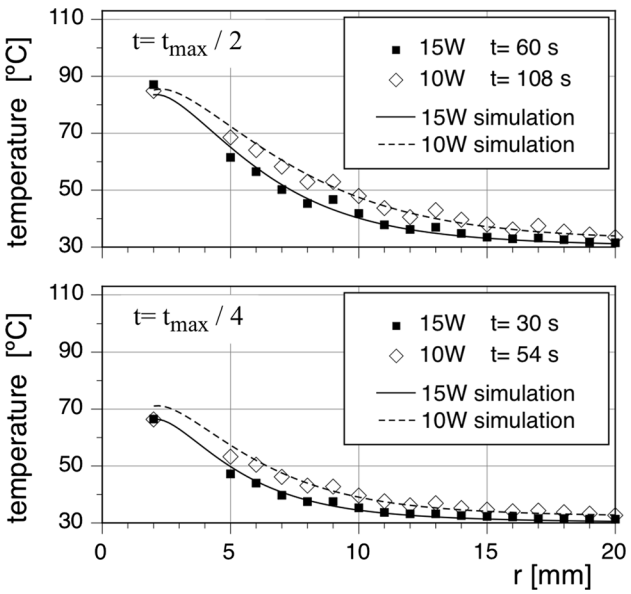

Fig. 7 Comparison between EQ 15 and EQ 10 radial temperature distributions at two fractional times ($1/2t_{max}$, $1/4t_{max}$): nails IR measurements (*markers*) and numerical simulation (*lines*). Despite the temperature distributions at the same fractional time are quite similar, the 10 W data always lay over the 15 W data: at low power the duration is longer and therefore conductive heat transfer is more effective

not considered. This hypothesis is a good approximation for capillary vessels; however, in liver tissue a lot of small but heat transport significant blood vessels (diame-ter $\geq$1 mm) are present and blood flow directionality should be taken into account [39]. For these reasons a more complex and more physically-based modeling approach is desired, in particular in view of patient specific RFTA planning [32, 33, 40]. The general idea is to use a one-dimensional flow model to describe the blood flow in the
large vessels (diameter $>$1 mm) and the Darcy model to describe the blood flow in microvessels [33, 40].

Preliminary simulations performed using an Arrhenius based perfusion model [36] showed that the effects of perfusion on the thermal lesion are particularly significant at low power and when the Joule heat source is more dif-fused in space (e.g., using hook-shaped electrodes and/or saline injection); at high power blood perfusion only extends the time required to obtain a given lesion volume. Nevertheless, as reported by Schutt and Haemmerich [36], different implementations of temperature dependent effects on perfusion and variations in baseline tissue perfusion have a considerable effect on ablation zone dimensions. It is evident that, for these reasons, the validation of in vivo RFTA models is fundamental. While using in vivo experiments is usually not feasible because of high costs, low repeatability and ethical issues, ex vivo perfused tests are increasingly used as a substitute that allows to avoid or at least to reduce these problems.

In contrast to thermal imaging, fiber optic sensors can be inserted in vivo through very small catheters. The increasingly rapid developments in this field could pave the way for a "smart-RFTA" scenario, where the ablation parameters can be automatically adapted during the procedure to optimize its efficiency [22]. More accurate temperature distribution measurements are underway: a very dense spacing can be achieved with the most recent generation of fiber optic distributed sensors [41], which make use of an interferometric setup to detect the Rayleigh back scattering within a single-mode optical fiber.

5 Conclusions

The results of the experiments described in this work allowed to define the main characteristics of the RF thermal lesion obtained on ex vivo porcine liver with tip-like active electrode. In particular, experimental evidence on the thermal field evolution close to the active tip was obtained and temperature gradients were measured inside the tissue. Numerical simulations based on a simple electro-ther-mal model allowed both to check the physical consistency of the measured data and to gain some insight on modeling the heating phase of the RF ablation. The results indicate that before the liquid–vapor phase change begins even a constant thermal conductivity model can correctly reproduce the measured temperature distributions. Further studies are underway to properly model the RFTA, including liquid–vapor phase change effects, and to measure more precisely the temperature distribution.

Acknowledgments This work was supported by the Italian Ministry of Education, University and Research (MIUR) through PRIN project "Metodi di misura e di simulazione numerica innovativi a supporto della termoablazione a radiofrequenza su tessuti parenchimali". The financial support of Ordine degli Ingegneri della Provincia di Pavia is gratefully acknowledged. The research is also supported by Fondazione Cura Mini-invasiva Tumori ONLUS.

References

1. Rossi S, Fornari F, Buscarini L (1993) Percutaneous ultrasound-guided radiofrequency electrocautery for the treatment of the small hepatocellular carcinoma. J Interv Radiol 8:97–103
2. Livraghi T, Goldberg SN, Lazzaroni S, Meloni F, Solbiati L, Gazelle GS (1999) Small hepatocellular carcinoma: treatment with radio-frequency ablation versus ethanol injection. Radiology 210:655–661
3. Rossi S, Ravetta V, Rosa L, Ghittoni G, Torello Viera F, Garbagnati F et al (2011) Repeated radiofrequency ablation for management of patients with cirrhosis with small hepatocellular carcinomas: a long term cohort study. Hepatology 53:136–147
4. Gervais DA, McGovern FJ, Arellano RS, McDougal WS, Mueller PR (2003) Renal cell carcinoma: clinical experience and technical success with radio-frequency ablation of 42 tumors. Radiology 226:417–424
5. Dupuy DE, Mayo-Smith WW, Abbott GF, DiPetrillo T (2002) Clinical applications of radio-frequency tumor ablation in the thorax. Radiographics 22:259–269
6. Zagoria RJ, Chen MY, Kavanagh PV, Torti FM (2001) Radiofrequency ablation of lung metastases from renal cell carcinoma. J Urol 166:1827–1828
7. Schulman CC, Zlotta AR, Rasor JS, Hourriez L, Noel JC, Edwards SD (1993) Transurethral needle ablation (TUNA): safety, feasibility, and tolerance of a new office procedure for treatment of benign prostatic hyperplasia. Eur Urol 24:415–423
8. Shinohara K (2004) Thermal ablation of prostate diseases: advantages and limitations. Int J Hyperth 20:679–697
9. Rosenthal DI, Hornicek FJ, Wolfe MW, Jennings LC, Gebhardt MC, Mankin HJ (1998) Percutaneous radiofrequency coagulation of osteoid osteoma compared with operative treatment. J Bone Joint Surg Am 80:815–821
10. Goldberg SN, Gazelle GS, Mueller PR (2000) Thermal ablation therapy for focal malignancy: a unified approach to underlying principles, techniques, and diagnostic imaging guidance. Am J Roentgenol 174:323–331
11. Goldberg SN, Gazelle GS, Dawson SL, Rittman WJ, Mueller PR, Rosenthal DI (1995) Tissue ablation with radiofrequency: effect of probe size, gauge, duration, and temperature on lesion volume. Acad Radiol 2:399–404
12. van Sonnenberg E, McMullen W, Solbiati L (2005) Tumor ablation: principles and practice. Springer, New York
13. Yang D, Converse MC, Mahvi DM, Webster JG (2007) Expanding the bioheat equation to include tissue internal water evaporation during heating. IEEE Trans Biomed Eng 54:1382–1388

14. Rossi S, Gallati M, Braschi G, Raboni M (2008) Modelling the liver RF thermal lesions. In: De Felice F (ed) Proceedings of the 17th IASTED international conference on applied simulation and modelling. ACTA Press, Calgary
15. Ai H, Wu S, Gao H, Zhao L, Yang C, Zeng Y (2012) Temperature distribution analysis of tissue water vaporization during microwave ablation: experiments and simulations. Int J Hyperth 28:674–685
16. Trujillo M, Alba J, Berjano E (2012) Relationship between roll-off occurrence and spatial distribution of dehydrated tissue during RF ablation with cooled electrodes. Int J Hyperth 28:62–68
17. Mulier S, Jiang Y, Wang C, Jamart J, Marchal G, Michel L, Ni Y (2012) Bipolar radiofrequency ablation with four electrodes: ex vivo liver experiments and finite element method analysis: influence of inter-electrode distance on coagulation size and geometry. Int J Hyperth 28:686–697
18. Gallati M, Braschi G (2013) On the simulation of radio frequency thermal lesions in porcine liver.In: Proceedings of the 32nd IASTED international conference on modelling, identification and control. doi:10.2316/P.2013.794-032
19. Watanabe H, Yamazaki N, Isobe Y, Lu X, Kobayashi Y, Miyashita T, Ohdaira T, Hashizume M, Fujie MG (2012) Validation of accuracy of liver model with temperature-dependent thermal conductivity by comparing the simulation and in vitro RF ablation experiment. Conf Proc IEEE Eng Med Biol Soc. doi:10.1109/EMBC.2012.6347292
20. Haemmerich D, Schutt DJ (2011) RF ablation at low frequencies for targeted tumor heating: in vitro and computational modeling results. IEEE Trans Biomed Eng 58:404–410
21. Tosi D, Macchi EG, Braschi G, Gallati M, Cigada A, Poeggel S, Leen G, Lewis E (2014) Monitoring of radiofrequency thermal ablation in liver tissue through fibre Bragg grating sensors array. Electron Lett 50:981–983
22. Tosi D, Macchi EG, Gallati M, Braschi G, Cigada A, Rossi S, Leen G, Lewis E (2014) Fiber-optic chirped FBG for distributed thermal monitoring of ex vivo radiofrequency ablation of liver. Biomed Opt Express 5:1799–1811
23. Diakides NA, Bronzino JD (2007) Medical Infrared Imaging. CRC Press, Boca Raton
24. Doebelin EO (1990) Measurement systems: application and design. McGraw-Hill, New York
25. JCGM 100:2008 (2008) Evaluation of measurement data—guide to the expression of uncertainty in measurement. Joint Committee for Guides in Metrology
26. Zurbuchen U, Holmer C, Lehmann KS, Stein T, Roggan A, Seifarth C, Buhr HJ, Ritz JP (2010) Determination of the temperature-dependent electric conductivity of liver tissue ex vivo and in vivo: importance for therapy planning for the radiofrequency ablation of liver tumours. Int J Hyperth 26:26–33
27. OpenFOAM, OpenCFD Ltd. http://www.openfoam.org. Accessed 15 Sept 2014
28. Duck FA (1990) Physical properties of tissues. Academic Press, San Diego
29. Choi J, Morrissey M, Bischof JC (2013) Thermal processing of biological tissue at high temperatures: impact of protein denaturation and water loss on the thermal properties of human and porcine liver in the range 25–80 °C. J Heat Transf 135:061302
30. Haemmerich D, dos Santos I, Schutt DJ, Webster JG, Mahvi DM (2006) In vitro measurements of temperature-dependent specific heat of liver tissue. Med Eng Phys 28:194–197
31. Shackelford JF, Alexander W (2001) CRC materials science and engineering handbook. CRC Press, Boca Raton
32. Paulides MM, Stauffer PR, Neufeld E, Maccarini PF, Kyriakou A, Canters RA, Diederich CJ, Bakker JF, Van Rhoon GC (2013) Simulation techniques in hyperthermia treatment planning. Int J Hyperth 29:346–357
33. Payne S, Flanagan R, Pollari M, Alhonnoro T, Bost C, O'Neill D, Peng T, Stiegler P (2011) Image-based multi-scale modelling and validation of radio-frequency ablation in liver tumours. Philos Trans A Math Phys Eng Sci 369:4233–4254
34. Pennes HH (1948) Analysis of tissue and arterial blood temperature in the resting human forearm. J Appl Physiol 1:93–122
35. Ahmed M, Liu Z, Humphries S, Goldberg SN (2008) Computer modeling of the combined effects of perfusion, electrical conductivity, and thermal conductivity on tissue heating patterns in radiofrequency tumor ablation. Int J Hyperth 24:577–588
36. Schutt DJ, Haemmerich D (2008) Effects of variation in perfusion rates and of perfusion models in computational models of radio frequency tumor ablation. Med Phys 35:3462–3470
37. Chang IA (2010) Considerations for thermal injury analysis for RF ablation devices. Open Biomed Eng J 4:3–12
38. Trujillo M, Berjano E (2013) Review of the mathematical functions used to model the temperature dependence of electrical and thermal conductivities of biological tissue in radiofrequency ablation. Int J Hyperth 29:590–597
39. Baish JW (2006) Microvascular Heat Transfer. In: Bronzino JD (ed) Tissue engineering and artificial organs. CRC Press, Boca Raton
40. He Y, Liu H, Himeno R, Sunaga J, Kakusho N, Yokota H (2008) Finite element analysis of blood flow and heat transfer in an image-based human finger. Comput Biol Med 38:555–562
41. Luna Inc. http://lunainc.com/obr4600ts. Accessed 15 Sept 2014